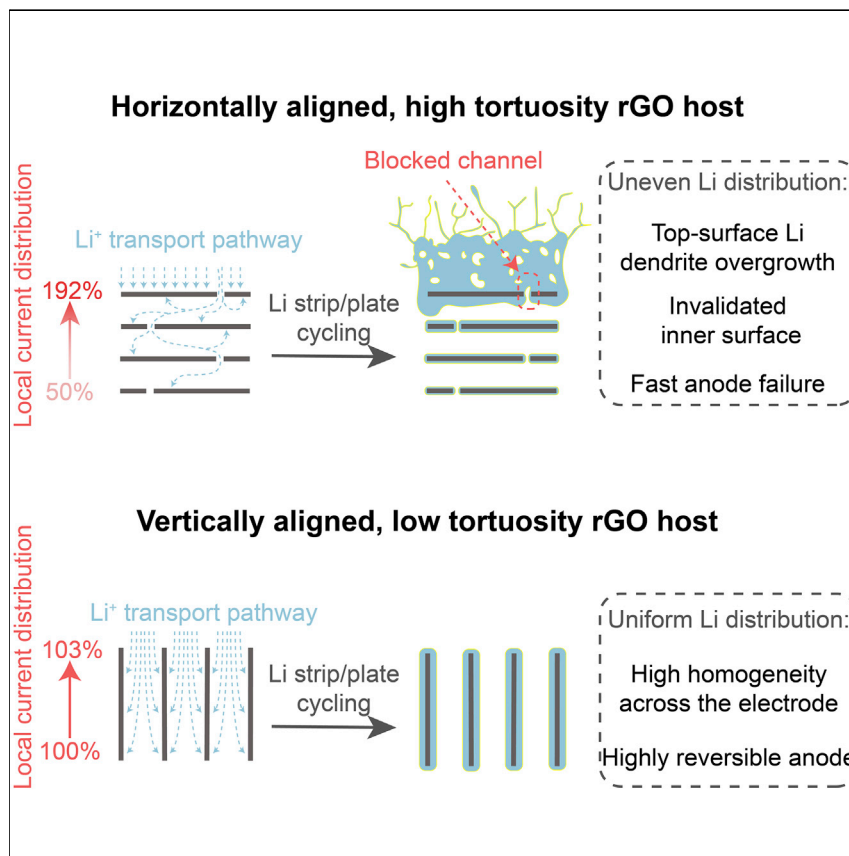


## Article

# Tortuosity Effects in Lithium-Metal Host Anodes



A strong correlation between host tortuosity and cycling reversibility of a hosted Li-metal anode is revealed for the first time. High tortuosity leads to preferential top-surface Li deposition based on locally enhanced current density and concentration gradient. This top-surface accumulated Li blocks inward ion transport and invalidates the internal electrode, further aggravating the uneven current distribution and non-uniform plating and stripping. Decreased electrode tortuosity can significantly improve the anodic Coulombic efficiency, uniformity of Li-metal stripping and plating, and cycling stability of the rGO host.

Hao Chen, Allen Pei, Jiayu Wan, ..., Yecun Wu, Hansen Wang, Yi Cui

yicui@stanford.edu

## HIGHLIGHTS

Controllable alignment and tortuosity in Li-metal host

Low tortuosity mitigates locally enhanced concentration gradient and current density

Suppress uneven Li dendrite overgrowth on top surface by decreasing host tortuosity

Strong correlation between host tortuosity and reversibility of hosted Li-metal anode



## Article

# Tortuosity Effects in Lithium-Metal Host Anodes

Hao Chen,<sup>1</sup> Allen Pei,<sup>1</sup> Jiayu Wan,<sup>1</sup> Dingchang Lin,<sup>1</sup> Rafael Vilá,<sup>1</sup> Hongxia Wang,<sup>1</sup> David Mackanic,<sup>3</sup> Hans-Georg Steinrück,<sup>4</sup> William Huang,<sup>1</sup> Yuzhang Li,<sup>1</sup> Ankun Yang,<sup>1</sup> Jin Xie,<sup>1</sup> Yecun Wu,<sup>1</sup> Hansen Wang,<sup>1</sup> and Yi Cui<sup>1,2,5,\*</sup>

## SUMMARY

Lithium (Li) metal is the ultimate anode material for Li batteries because of its highest capacity among all candidates. Recent research has focused on stable interphase and host materials to address its low stability and reversibility. Here, we discover that tortuosity is a critical parameter affecting the morphology and electrochemical performances of hosted Li anodes. In three types of hosts—vertically aligned, horizontally aligned, and random reduced graphene oxide (rGO) electrodes with tortuosities of 1.25, 4.46, and 1.76, respectively—we show that high electrode tortuosity causes locally higher current density on the top surface of electrodes, resulting in thick Li deposition on the surface and degraded cycling performance. Low electrode tortuosity in the vertically aligned rGO host enables homogeneous Li transport and uniform Li deposition across the host, realizing greatly improved cycling stability. Using this principle of low tortuosity, the designed electrode shows through-electrode uniform morphology with anodic Coulombic efficiency of ~99.1% under high current and capacity cycling conditions.

## INTRODUCTION

Rapid developments in portable electronic devices and electric vehicles have brought about an urgent need for high-energy-density rechargeable lithium-ion batteries.<sup>1,2</sup> High-specific-capacity anodes<sup>3</sup> as alternatives to the existing graphite, such as silicon (Si)<sup>4</sup> and most recently lithium (Li) metal,<sup>5,6</sup> have been intensely studied. Li metal is regarded as the ultimate choice of anode because it has the highest theoretical capacity (3,860 mAh g<sup>-1</sup>) and lowest electrode potential (-3.04 V versus the standard hydrogen electrode). However, it is now widely recognized that Li-metal anodes exhibit severe drawbacks such as undesired dendritic growth,<sup>7–9</sup> low Coulombic efficiency (CE), fast capacity fading, increased voltage hysteresis, and dead Li formation, which we believe result from two key causes: high chemical reactivity and relative infinite volume changes during plating and stripping.

Extensive research efforts that have been devoted to tackling these problems can be categorized according to the two root causes. One set of ideas aims to develop a stable interphase with Li metal, including inorganic interphases (such as hollow carbon spheres,<sup>10</sup> LiF,<sup>11</sup> diamond,<sup>12</sup> and Li<sub>3</sub>PO<sub>4</sub><sup>13</sup>), organic interphases (such as strong and soft polymers<sup>14,15</sup>), and interphases formed by screening the electrolyte and additives.<sup>16–18</sup> The chemical and mechanical stability of the interphase was proposed and demonstrated as a critical design principle.<sup>10,19</sup> Atomic resolution of the Li-metal interphase can now be obtained through cryogenic electron microscopy imaging and correlated with electrochemical performance.<sup>20</sup> Interfacial engineering

## Context & Scale

Host electrodes, such as three-dimensional (3D) porous carbon matrices, can accommodate the relative infinite volume change and decrease the local current density for mitigating dendritic growth and reversibility issues in a Li-metal anode. However, a preferential Li accumulation on the upper surface of the host is commonly observed during cycling, which has not been rationalized or addressed. Here, we show that the host tortuosity, as a complexity of the microstructure inside the 3D host, is responsible for this uneven Li distribution. In comparisons between rGO hosts with different tortuosities, the locally enhanced current density and concentration gradient showed a strong correlation with high host tortuosity, leading to top-surface accumulation of Li dendrites and a blocked ion-transport pathway. When the host tortuosity was reduced from 4.46 to 1.25, rGO hosts exhibited a doubled cycle life in full cells with high uniformity within the anode, suggesting the importance of this tortuosity parameter for stable Li-metal batteries.



continues to be important through the guidance of atomic structure understanding. The other set of ideas focuses on developing materials as hosts for containing Li metal within. Ideas include seeded hollow carbon spheres,<sup>21</sup> three-dimensional (3D) carbonaceous electrodes,<sup>22,23</sup> 3D porous metallic structures,<sup>24–27</sup> over-lithiated SiO<sub>x</sub>, and metal fluorides.<sup>28,29</sup> These host structures reduce the electrode-level volume fluctuation by ~10 times and enhance stability by localizing the global volume changes (15–30 μm for 3–6 mAh cm<sup>-2</sup>) to the local domain of Li metal.

To make further progress in the development of Li-metal anodes, we would like to bring the attention of the research community to a phenomenon commonly observed in hosted Li-metal anodes: preferential Li accumulation on the upper surface of the whole electrode during deposition.<sup>30,31</sup> This preferential accumulation of Li metal creates a larger volume expansion in the top part of electrodes than in the lower parts and blocks Li-ion diffusion down into the lower part of the electrode. This uneven deposition of Li could cause host material anodes to fail over cycling. To date, the source and solutions for this non-uniform deposition in Li-metal anodes remain elusive and unexplored, especially in the Li-metal anode field, which we can learn from the preliminary Li-plating phenomenon in fast-charging graphite anode materials.<sup>32,33</sup>

Here, we propose that the tortuosity at the electrode level is one of the most important factors for generating such an uneven distribution of Li-metal deposition. Tortuosity is a diffusional parameter describing the complexity of ionic or mass transport in the porous electrode network and is affected by the geometrical complexity of the microstructure inside the 3D porous electrode. Tortuosity affects transport properties, liquid-phase diffusivity, and conductivity:

$$K_{\text{eff}} = \frac{K\epsilon}{\tau} \quad (\text{Equation 1})$$

$$D_{\text{eff}} = \frac{D\epsilon}{\tau} \quad (\text{Equation 2})$$

Here,  $\epsilon$  is the porosity;  $K_{\text{eff}}$  and  $K$  are the effective and intrinsic conductivities, respectively; and  $D_{\text{eff}}$  and  $D$  are the effective and intrinsic diffusivities, respectively, of the conductive phase (in the present case, the liquid electrolyte inside porous electrode).<sup>34–36</sup> Equations 1 and 2 serve as the definition of tortuosity ( $\tau$ ) used in the present work. With higher tortuosity, Li-ion-transportation paths within the electrode will be extended. Notably, the tortuosity has been recognized as an important parameter for conventional graphite anodes, affecting Li concentration gradients during operation while manifesting even more severely during fast charging.<sup>32,33,37,38</sup> Accordingly, low tortuosity graphite electrode structures have been proposed and developed.<sup>39</sup> However, we hypothesize that compared with graphite, the electrode tortuosity could have more critical effects on Li-metal plating. This is because plating at any particular location of Li metal can continue indefinitely, whereas Li intercalation capacity in any particular graphite particle is stoichiometrically limited to fully lithiated LiC<sub>6</sub> (if the Li-metal plating potential not exceeded). We expect that high-tortuosity electrodes would have current density primarily distributed to the upper part of electrodes, resulting in localized preferential accumulation of Li metal, whereas low-tortuosity electrodes would have more uniform current distribution and thus Li deposition across the entire thickness of the electrode.

Although the above proposed hypothesis might seem intuitive, there has not been any clear demonstration of the effect of tortuosity on Li-metal morphology and

<sup>1</sup>Department of Materials Science and Engineering, Stanford University, Stanford, CA 94305, USA

<sup>2</sup>SLAC National Accelerator Laboratory, Stanford Institute for Materials and Energy Sciences, 2575 Sand Hill Road, Menlo Park, CA 94025, USA

<sup>3</sup>Department of Chemical Engineering, Stanford University, Stanford, CA 94305, USA

<sup>4</sup>SSRL Materials Science Division, SLAC National Accelerator Laboratory, Menlo Park, CA 94025, USA

<sup>5</sup>Lead Contact

\*Correspondence: [yicui@stanford.edu](mailto:yicui@stanford.edu)

<https://doi.org/10.1016/j.joule.2020.03.008>

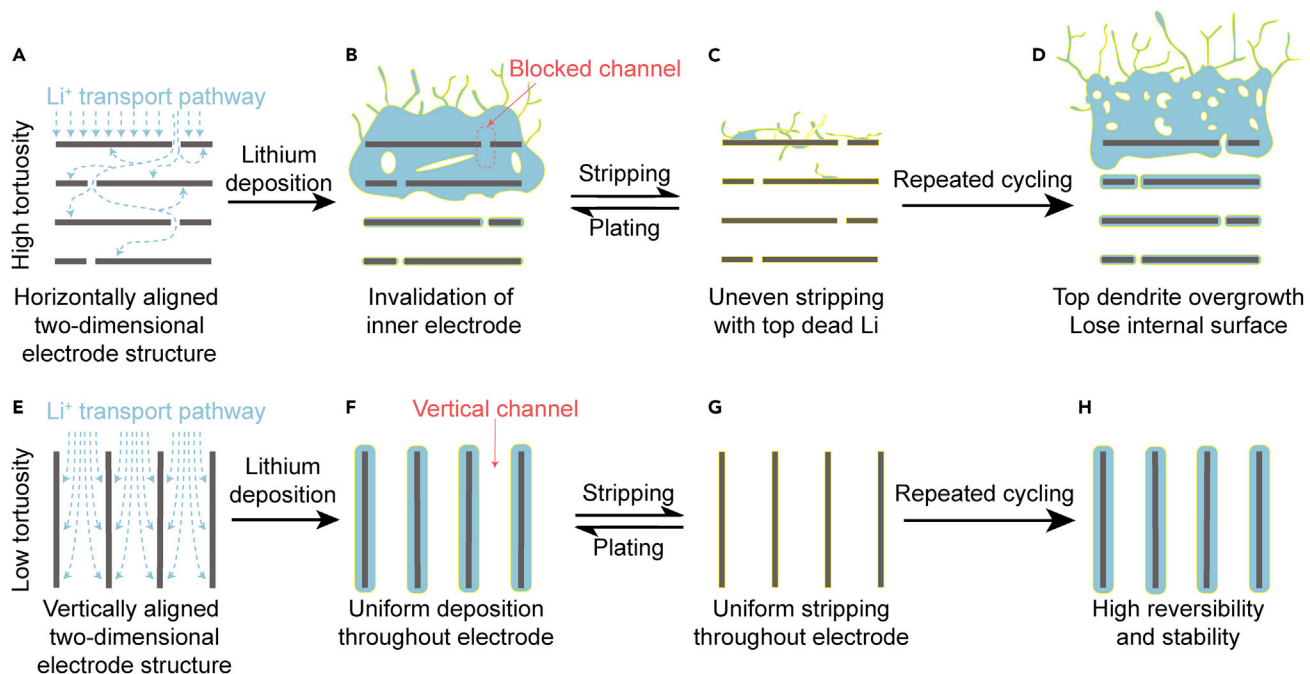


**Figure 1. Schematic of the Effect of Tortuosity on the Structure Evolution of Li-Metal Anodes during Cycling**

- (A) During electrochemical plating, Li metal prefers to deposit on the top of high-tortuosity electrodes through short ion-transport paths.
- (B) Accumulated Li on top can also block the inward ion-transport pathways into the electrode and inactivate internal electrode surfaces, further favoring dendritic overgrowth on top.
- (C) The accumulated Li dendrites turn into dead Li and SEI after stripping as a result of locally enhanced current density, which generates large amounts of Li loss and also blocks inward ion-transport paths in turn.
- (D) After repeated channel blockage and loss of effective surface from cycling together with dead Li accumulation on top, deposited Li dendrites all agglomerate on the top surface of the electrode, leading to anode failure.
- (E and F) Because of the low tortuosity of the vertically aligned 2D graphene electrode, Li can be uniformly deposited into an electrode with a large effective surface area without blocking ion-transport paths.
- (G) Because of the low electrode tortuosity, Li can be evenly stripped without dead Li.
- (H) After repeated cycling, the low-tortuosity electrode can maintain good stability and reversibility because of the absence of channel blockage, effective area loss, locally enhanced current density, or dead Li behavior.

electrochemical behavior. In this report, we have developed the controlled tortuosity of a reduced graphene oxide (rGO) host over a very large range of values. When using these rGO hosts for Li-metal deposition, we demonstrated the clear relationship between tortuosity and Li-metal anode structure and performance. As exhibited in Figure 1A, metallic Li tends to be deposited and stripped at the upper surface of highly tortuous electrodes (especially horizontally aligned layered rGO) because of the much longer ion-transport pathways to the middle or bottom part of the electrode. Over time, the accumulated Li on the top further impedes ionic transport by physically blocking electrolyte access to the internal electrode, in turn aggravating upper overgrowth, solid-electrolyte interphase (SEI) fracture, and loss of the effective internal electrode surfaces (Figure 1B). After stripping, the high electrode tortuosity and decreased surface lead to locally enhanced current density with increased amounts of residual dead Li particles and SEI on the upper surface, which further degrade anode reversibility, block inward ion-transport pathways, and exacerbate uneven Li accumulation (Figure 1C). Suffering from this vicious cycle, carefully designed multilevel electrode structures and Li-protection strategies become counterproductive, leading to fast failure of the Li-metal anode (Figure 1D). In comparison, the vertically aligned, ultralow-tortuosity rGO electrode generates very straight, direct, inward Li-ion-transport paths (Figure 1E), enabling highly

reversible uniform Li delivery into the electrode without any upper overgrown Li (Figures 1F–1H).

Experimentally, we found that the horizontally aligned, highly tortuous rGO electrodes exhibited a severe 80- $\mu\text{m}$ -thick upper overgrowth of dendrites after a single plating step, rapid anodic CE decay from 98.6% to 90% after only 24 cycles, and fast full-cell failure within 200 cycles. The vertically aligned low-tortuosity electrodes exhibited greatly improved electrochemical performance: a high anodic CE of  $\sim$ 99.1% within 150 cycles, through-electrode uniform Li deposition, and 400 stable full-cell cycles even under high current density, high areal capacity, and limited Li conditions. Our simulation results also support that the lower electrode tortuosity generates a significantly decreased Li-ion concentration gradient in the electrolyte and enables nearly homogeneous electrode current density (only 3.6% higher current at the surface of vertical rGO as compared with 283% higher for horizontal rGO), suggesting the necessity of low electrode tortuosity for stable Li-metal anodes.

## RESULTS AND DISCUSSION

### Fabrication and Characterization of Electrodes

To generate the controllable alignment of rGO host electrodes, we adopted a method of unidirectional freezing and ice-segregation-induced assembly of two-dimensional (2D) graphene oxide (GO) sheets, initially demonstrated by the Bechtold group (Figure 2A).<sup>40–42</sup> GO aqueous solution was filled into a polyimide O-ring mold and transferred onto a cold plate (Figure S1). Ice rapidly grows perpendicularly to the cold surface, forcing the 2D GO sheets to align vertically in the boundaries between adjacent and oriented 20  $\mu\text{m}$  ice crystals, as revealed by *in situ* optical microscopy (Figures S1D–S1F; Video S1). During the subsequent vacuum-drying process, the oriented ice was sublimated, leaving behind empty aligned channels formed from the surrounding aligned GO sheet walls inside the vertically aligned GO aerogel (VGOA). After further annealing reduction on VGOA, the vertically aligned rGO aerogel (VGA) electrodes can be fabricated at large scales with perpendicular channels and lithophilic electronically conducting rGO walls. Similarly, horizontally aligned rGO aerogel (HGA) electrodes were also fabricated by unidirectional freezing from the side instead of from the bottom, exhibiting horizontally aligned rGO walls and channels (Figure 2B). In addition, conventional randomly arranged rGO aerogel (RGA) electrodes were also fabricated by an all-directional freezing procedure in liquid nitrogen (Figure 2C) followed by the same vacuum-drying and annealing-reduction processes, which resulted in randomly arranged rGO sheets and channels without preferentially aligned features.<sup>43,44</sup> The densities of all kinds of prepared rGO aerogel (GA) electrodes were all measured to be around 3.5 mg mL<sup>−1</sup>, revealing similarly high  $\sim$ 99.8% electrode porosities ( $\epsilon$ ) that allow for plenty of space for Li storage along with neglectable compromise to the energy density of the anode.

The vertically oriented channeled structure of VGA was first revealed by cross-sectional scanning electron microscopy (SEM; Figure S2A), exhibiting millimeter-scale continuous vertical alignment. Magnified cross-sectional SEM images show that these frames are constructed by vertically oriented, continuous, and nanometer-thick walls surrounding inner void channels ( $\sim$ 20  $\mu\text{m}$  wide; Figures 2D and S2), which are consistent with the transmission electron microscopy (TEM) images (showing several-nanometer-thick, four-layer rGO wall with interlayer spacing of 0.34 nm; Figure S3) and *in situ* optical microscopy images (showing internal ice crystal of around 20  $\mu\text{m}$  width; Figure S1F). The top-view SEM images of VGA exhibited a

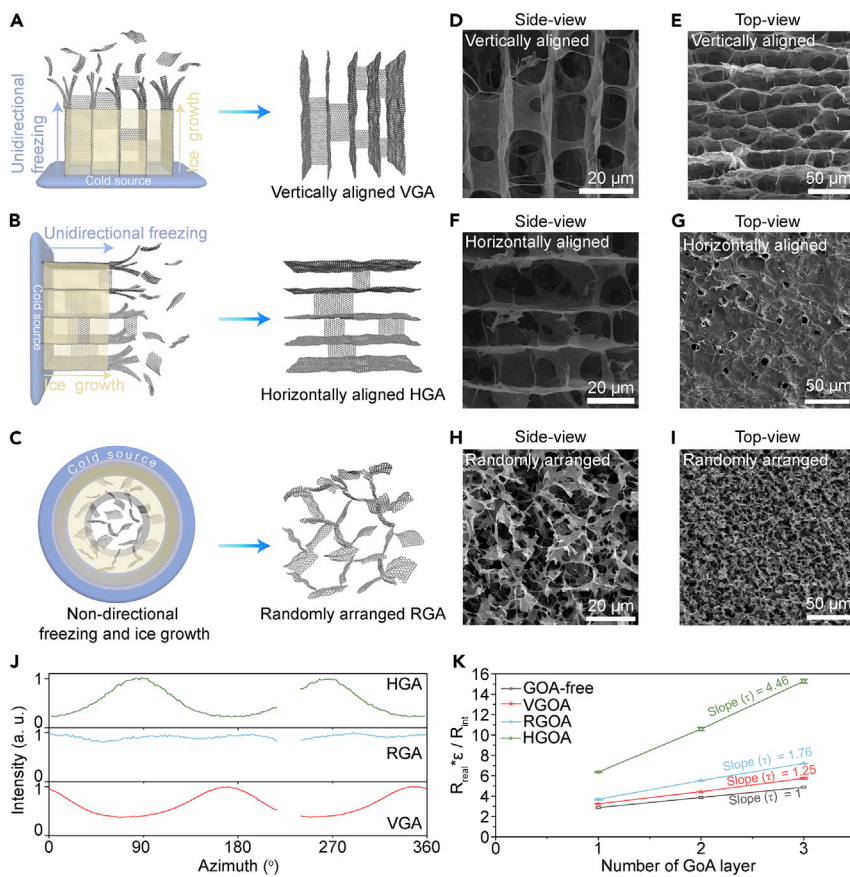


**Figure 2. Characterizations of GA Electrodes**

- (A) Schematic of fabrication of VGA electrode.
- (B) Schematic of fabrication of HGA.
- (C) Schematic of fabrication of RGA.
- (D and E) Cross-sectional (D) and top-view (E) SEM images of VGA.
- (F and G) Cross-sectional (F) and top-view (G) SEM images of HGA.
- (H and I) Cross-sectional (H) and top-view (I) SEM images of RGA.
- (J) SAXS measurements of different GA electrodes.
- (K) Tortuosity measurements ( $\tau$ ) of different electrolyte-infiltrated, electronic-insulated GOAs via ionic resistance measurements.  $R_{\text{real}}$ , areal high-frequency real resistance extracted from Figure S8;  $R_{\text{int}}$ , intrinsic ionic resistance;  $\epsilon$ , porosity. Detailed calculation steps can be observed from Figure S8. Assuming no structure change during reduction of GOA, the tortuosity of GOA should be the same with the corresponding GA electrodes after thermal reduction.

matrix-like arrangement of the nanometer-thick edges of vertical rGO walls, and no horizontal rGO surfaces could be observed (Figure 2E). These vertical channels and horizontal surface-free structures provide ideal perpendicular and direct ion-transportation pathways into the electrode, representing low electrode tortuosity. In consideration of the electrode volumetric energy density, thin VGA can be also fabricated by reducing the mold thickness, achieving an electrode with thickness of  $\sim 125 \mu\text{m}$  as demonstration for a thin electrode that still maintains good vertical alignment (Figure S4). In comparison with the vertically aligned channeled structure of VGA, the HGA exhibited a similar aligned structure but with different orientation; most rGO sheets and channels are horizontally aligned and lie parallel to the top surface (Figures 2F and S5). Top-view SEM images indicate a continuous horizontal rGO surface with few holes or vertical channels for ion infiltration into the electrode (holes occupy 1.32% of area and are on average  $11 \mu\text{m}^2$  in size calculated by ImageJ;

([Figures 2G](#) and [S5C](#)). These nearly hole-free, horizontally aligned rGO walls can significantly block inward ion transport, leading to the high electrode tortuosity of HGA. In contrast, the RGA exhibited a different structure with rGO sheets randomly arranged with abundant holes and vertical channels for ion transport, and no apparent alignment directions were observed ([Figures 2H](#) and [2I](#)). Even though these perpendicular channels provide abundant pathways for inward ion transport, the randomly arranged rGO sheets can still impede ion transport to a certain extent, leading to a slightly increased electrode tortuosity in RGA. Small-angle X-ray scattering (SAXS) measurements further confirmed these tunable alignments in GA electrodes. VGA and HGA exhibited anisotropic scattering at angles of nearly 90° and 180°, respectively, indicating bulk vertical and horizontal alignment of the rGO sheets ([Figure 2J](#)). In contrast, the RGA exhibited no apparent periodic increases in scattering intensity, demonstrating the absence of alignment ([Figure S6](#)).<sup>45</sup>

Although the various GA electrodes exhibited no apparent differences in chemical composition, as confirmed by X-ray diffraction (XRD) and X-ray photoelectron spectroscopy (XPS) spectra ([Figure S7](#)), their tortuosities were significantly different. We followed an electrochemical method previously developed by the Gasteiger group to determine the tortuosity of separators.<sup>35</sup> By measuring the high-frequency ionic resistances of electrolyte-infiltrated insulated graphene oxide aerogels (GOAs, before annealing reduction; [Figures 2K](#) and [S8](#)),<sup>35,36</sup> the tortuosity of VGOA was calculated to be 1.25. The randomly arranged GOA (RGOA) exhibited a slightly increased tortuosity of 1.76, whereas horizontally aligned GOA (HGOA) showed a high tortuosity of 4.46, suggesting a significantly increased length of ion-transport pathways. Considering that there is no structural change during GOA reduction, the tortuosity of GOA should be same with the corresponding GA electrodes after thermal reduction. The significantly increased tortuosities in different GA electrodes were also qualitatively supported by the polarization-interrupt measurement on different GA electrodes, indicating that VGA and HGA have the lowest and highest tortuosities, respectively ([Figure S8F](#)),<sup>34,36</sup> which is consistent with previous SEM images. These data illustrate that the biggest differences between vertical, horizontally aligned, and randomly arranged electrodes lie in their tortuosity and aligned structures, which can be directly applied to characterize the influence of tortuosity on the reversibility of hosted Li-metal anodes.

### Electrochemical Performances

The effects of electrode tortuosity on electrochemical performance were evaluated by CE cycling tests (see [Experimental Procedures](#) for detail; [Figure 3](#)), which determined the reversibility of galvanostatic Li plating and stripping on different electrodes at various current densities and capacities. The counter electrode was Li-metal foil. In the CE test under typical cycling conditions (current density of 1 mA cm<sup>-2</sup> and capacity of 1 mAh cm<sup>-2</sup> with the same amount of 50 µL ether electrolyte of 1 M Li bis(trifluoromethanesulfonyl)imide (LiTFSI) in 1:1 [v/v] 1,3-dioxolane [DOL]/dimethyl ether [DME] electrolyte with 1% LiNO<sub>3</sub> additive; [Figure 3A](#)), the highly tortuous HGA electrode exhibited a lower CE of ~96.7% with higher overpotential of 34 mV and fast decay after 120 cycles, whereas the medium tortuosity RGA electrode showed a higher CE of ~97.4% with medium overpotential of ~30 mV and slightly better stability over 150 cycles. In comparison, the low tortuosity VGA electrode achieved the most stable CE of ~99.1% with nearly identical voltage profiles over 300 cycles (small overpotential of 19 mV; [Figure S10A](#)). These data prove that the low-tortuosity feature does enable uniform Li delivery and improves cycling stability of the Li-metal anode.

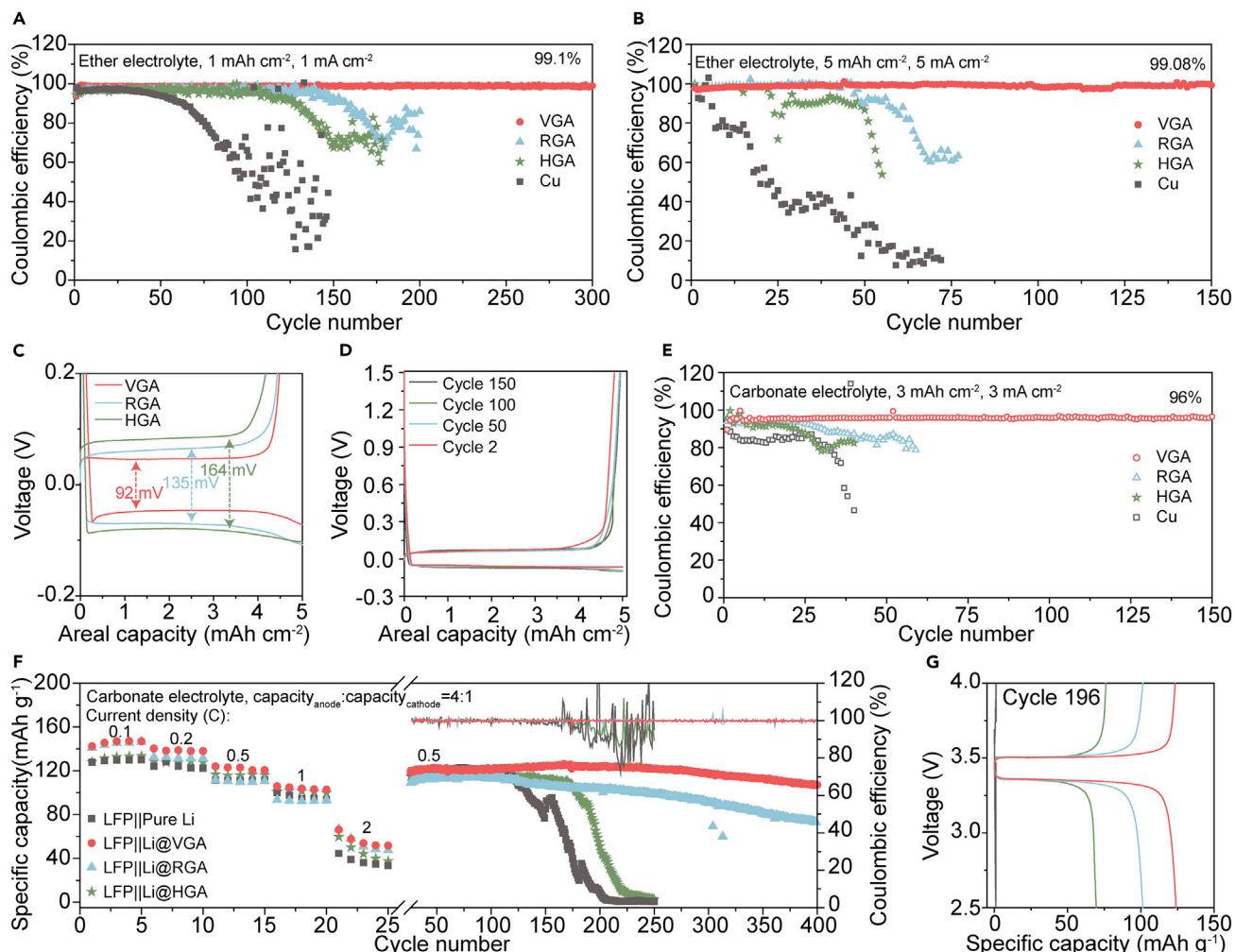


**Figure 3. Electrochemical Performances of the GA Anodes**

- (A) Li cycling CE on different anodes with ether electrolyte at a current density of 1 mA cm<sup>-2</sup> and a capacity of 1 mAh cm<sup>-2</sup>.
- (B) Li cycling CE on different anodes with ether electrolyte at a current density of 5 mA cm<sup>-2</sup> and a capacity of 5 mAh cm<sup>-2</sup>.
- (C) Corresponding voltage-versus-capacity plot of different electrodes at first cycle using ether electrolyte.
- (D) Corresponding voltage-versus-capacity plot of VGA electrode during different cycles using ether electrolyte.
- (E) Li cycling CE on different anodes with carbonate electrolyte at a current density of 3 mA cm<sup>-2</sup> and a capacity of 3 mAh cm<sup>-2</sup>.
- (F) Rate capability and long-term cycling performances of LFP||Li cells with different anodes (limited amount of Li-metal anode, ~10 mAh cm<sup>-2</sup>) and high-loading LFP cathode (16 mg cm<sup>-2</sup>, ~2.5 mAh cm<sup>-2</sup>), resembling 25% utilization of anode in each cycle. 1 C = 170 mA g<sup>-1</sup>.
- (G) Corresponding voltage-versus-specific capacity plot of LFP full cells using different anodes at the 196<sup>th</sup> cycle.

Considering the high-energy-density and fast-charging demands on future batteries, stable performance of Li-metal anodes must be achieved, especially under high-capacity and high-current-density cycling conditions. When the cycling current density and areal capacity were increased to 5 and 5 mAh cm<sup>-2</sup>, respectively, in ether electrolyte, the HGA electrode only reached 24 cycles before CE decayed from 98.6% to 90%, whereas the RGA electrode exhibited 48 stable cycles before CE decayed from 99% to 90%. In contrast, the VGA electrode maintained a stable CE averaging ~99.08% even in the last 20 cycles after 150 cycles (Figure 3B). Such a significantly improved anode CE in ether electrolyte system benefits the future ether electrolyte-based high-energy-density Li-S and Li-air battery systems, which require highly reversible Li stripping and plating in ether electrolyte under high-current-density and high-areal-capacity cycling conditions. In the voltage-capacity plot,

VGA exhibited an obvious lower overpotential (46 mV) than the higher-tortuosity RGA (67.5 mV) and HGA (82 mV; Figure 3C), demonstrating that tortuosity also has a large impact on electrode kinetics. In addition, both HGA and RGA showed obvious overpotential increases from 82 to 114 mV and 67.5 to 95 mV, respectively, after cycling (Figure S12), whereas VGA maintained a stable overpotential of ~46 mV and exhibited overlapped voltage profiles (Figure 3D). Such tortuosity-dependent anode-stability phenomena were also observed under common cycling conditions for traditional Li-ion batteries in carbonate electrolyte (1 M LiPF<sub>6</sub> in 1:1 [v/v] ethylene carbonate [EC] and diethyl carbonate [DEC] with 1% vinylene carbonate [VC] and 10% fluoroethylene carbonate [FEC] as additives, current density of 3 mA cm<sup>-2</sup>, capacity of 3 mAh cm<sup>-2</sup>). The HGA and RGA showed lower CEs of 91.8% and 93.7% with fast CE decay after only 28 and 55 cycles, respectively (later decaying lower than 80%), along with greatly increased overpotential (from 97 to 356 mV for RGA after 60 cycles [Figure S14B] and from 101 to 437 mV for HGA after 40 cycles [Figure S14C]). Meanwhile, the VGA exhibited a stable CE of around 96% with stable voltage profiles even after 150 cycles, along with a smaller amount of overpotential variation (76 to 148 mV after 150 cycles; Figure S14D). These performance comparisons between different GA electrodes demonstrate that low electrode tortuosity significantly improves electrochemical stability and reversibility of Li-metal anodes.

Benefiting from the low-electrode-tortuosity principle, the performances of full cells were significantly improved especially under limited Li conditions (10 mAh cm<sup>-2</sup>, pre-stored into rGO hosts by electrochemical deposition). With high mass loading Li iron phosphate (LFP) cathodes (~16.5 mg cm<sup>-2</sup>, ~2.5 mAh cm<sup>-2</sup>; Figure 3E), the full cells with GA host anodes exhibited better performances than those with pure Li-metal anodes, whereas the Li@VGA anode showed further improved full-cell capacity and rate capability over those of Li@RGA and Li@HGA because of the lower tortuosity and enhanced electrode kinetics (Figure S15A), which is consistent with previous overpotential data.<sup>46</sup> Importantly, the LFP||Li@VGA cell exhibited 90% capacity retention even after 400 cycles with stable voltage profiles, whereas the LFP||Li@RGA cell showed only 63% capacity retention and an obvious increase in overpotential after 400 cycles (Figure S15B). In comparison, the LFP||Li@HGA and LFP||pure Li full cells completely failed after 250 and 200 cycles, respectively. Considering that the LFP cathode has excellent reversibility,<sup>47</sup> the fading of the full-cell capacity should be attributed only to the Li loss at the highly tortuous anode side, which is consistent with previous CE cycling data and symmetric cell-cycling data (Figure S9). In a more practical LiNi<sub>0.6</sub>Mn<sub>0.2</sub>Co<sub>0.2</sub>O<sub>2</sub> (NMC622, 4.1 mAh cm<sup>-2</sup>)-based full cell with a lower anode/cathode capacity ratio of 1.22:1 (anode areal capacity of 5 mAh cm<sup>-2</sup>), the full cells using the Li@VGA anode showed stable cycling (86.7% capacity retention) after 150 cycles, surpassing those full cells with the pure Li-metal anode (1% capacity retention), Li@HGA anode (1% retention), and Li@RGA anode (9.45% retention; Figure S16). These data demonstrate the significance of low-tortuosity anode design for high-energy-density and stable Li-metal batteries.

#### Influence of Tortuosity on the Structure of Li-Metal Anodes

To elucidate the mechanisms behind the improved electrochemical performances, we compared the morphology evolution of different bare electrodes without pre-stored Li after CE test cycling in the commonly used carbonate electrolyte system, as the dendritic Li morphology is more obvious in the carbonate electrolyte system.<sup>48</sup> For tortuous HGA and RGA electrodes, Li ions are more preferentially electrochemically reduced and deposited on the top rGO layer surface after traveling the shortest ion-transport path (Figures 4A and 4B). Moreover, the deposited

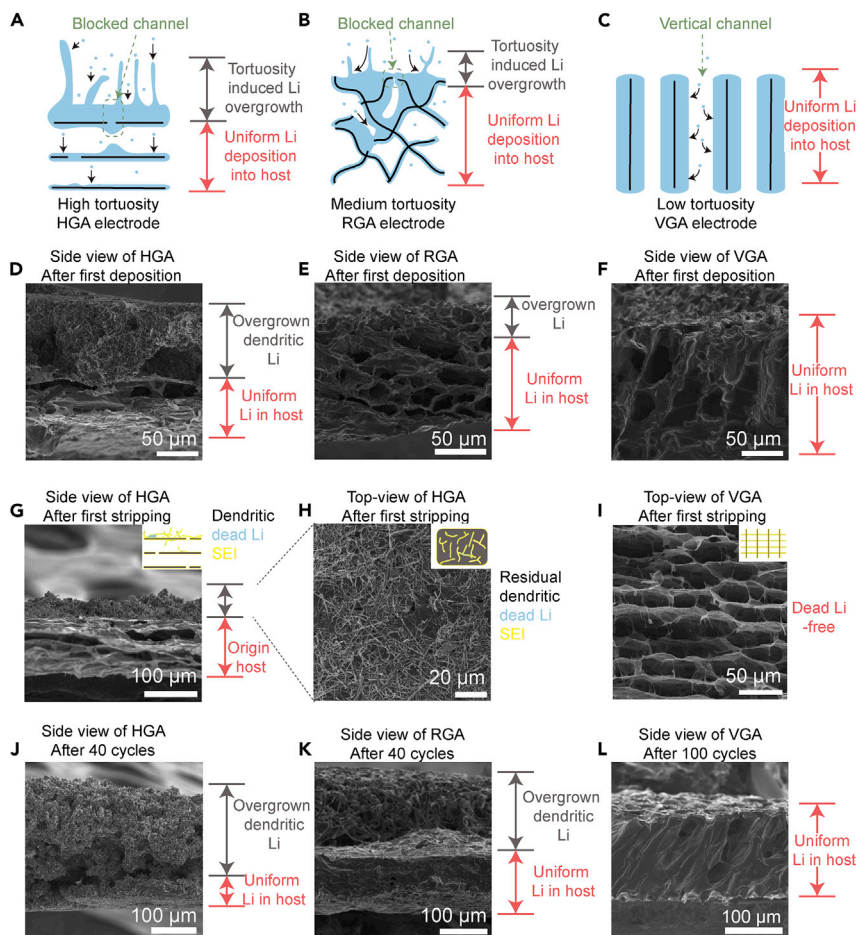


**Figure 4. Li-Deposition and Cycling Behavior in Different Anodes**

(A–C) Schematics of Li deposition in HGA (A), RGA (B), and VGA (C).

(D–F) Cross-sectional SEM images of HGA (D), RGA (E), and VGA (F) after the first Li-deposition step.

(G–H) Cross-sectional (G) and top-view (H) SEM images of HGA after the first Li-stripping step.

(I) Top-view SEM images of VGA electrode after the first Li-stripping step.

(J and K) Cross-sectional SEM images of HGA (J) and RGA (K) after 40 cycles. Insets show schematics of HGA and VGA after the stripping step.

(L) Cross-sectional SEM images of VGA after 100 cycles. The cycling current density and capacity were  $3 \text{ mA cm}^{-2}$  and  $3 \text{ mAh cm}^{-2}$ , respectively, in carbonate electrolyte.

Li can block the ion-transport pathways and in turn further increase electrode tortuosity. This leads to the loss of effective internal surface area and locally enhanced current density on the top of electrode, facilitating upper dendritic Li overgrowth. For the low-tortuosity VGA electrode, Li ions can transport through the short vertical channels to be uniformly electrochemically reduced and deposited onto the vertical rGO walls, which maintains the effective surface area and homogenizes the current density distribution (Figure 4C). During the first Li-deposition step in highly tortuous HGA, only small amounts of Li were observed to be uniformly coated onto the original 1-nm-thick rGO sheets inside the electrode, depositing in 2-μm-thick, evenly coated layers (Figures S18 and S19). Meanwhile, an 85-μm-thick layer of Li was accumulated on the top horizontal rGO surface (Figure 4D), showing dendritic morphology similar to that on copper electrodes (Figure S17). The medium-tortuosity RGA exhibited better uniformity such that most Li was deposited inside the

electrode, whereas a 40-μm-thick layer of surfacial accumulated Li particles was still observed ([Figures 4E](#) and [S20](#)). In comparison, for the low-tortuosity VGA, all Li was very uniformly deposited onto the vertical rGO walls inside the electrode, and no Li accumulated on the top surface ([Figures 4F](#), [S21](#), and [S22](#)). These variations in morphology directly demonstrate that the high electrode tortuosity severely aggravated the upper Li-overgrowth issues, leading to a locally drastic volume change and compromised SEI stability, which seriously degraded anode reversibility.

Importantly, after the subsequent stripping step, GA electrodes exhibited totally different morphologies of residual dead Li and SEI. As observed in the cross-sectional SEM image in [Figure 4G](#), ~36 μm of dendritic dead Li and SEI remained on the top rGO layer of HGA after the subsequent stripping step, which can be further confirmed in the top-view SEM image ([Figure 4H](#)). This behavior is very similar to that of the top horizontal surface copper electrode ([Figure S17H](#)). In contrast, no dead Li could be observed on top of or inside VGA, and the original vertical channeled structure was well retained ([Figures 4I](#) and [S23](#)). These results are also supported by XRD spectra, showing that the charged-state HGA and RGA electrodes have large and medium amounts of Li-metal residues, respectively, whereas the VGA electrode shows an absence of metallic Li residue at the charged state ([Figures S23C](#) and [S23D](#)). After a single Li plating-stripping cycle, the structures of GA electrodes exhibited more obvious deterioration in uniformity and larger amounts of dead Li with increased tortuosity, demonstrating that high electrode tortuosity does lead to larger amounts of Li loss, consistent with previous CE data. Suffering from this tortuosity-induced uneven distribution and Li loss, the highly tortuous HGA electrode exhibited 200 μm of top-accumulated Li dendrites with high roughness after 40 cycles ([Figures 4J](#) and [S24](#)), whereas the medium-tortuosity RGA electrode showed 125 μm of top-accumulated Li dendrites together with 117 μm of uniformly filled electrode at the bottom ([Figure 4K](#)). In comparison, all Li was evenly filled into the 135-μm-thick VGA electrode even after 100 cycles, illustrating its well-maintained vertical channeled structure along with an absence of surficial accumulation or dendritic morphology ([Figures 4L](#) and [S25](#)). These dramatic differences between GA electrodes demonstrate that high electrode tortuosities have significant detrimental impacts on the reversibility and morphology of Li-metal anodes, even if the electrodes possess the same chemical composition, porosity, and electrolyte and SEI components ([Figure S26](#)). Hence, low electrode tortuosity is a must for stable and reversible Li-metal anodes.

### Simulation Results

To further reveal the key roles of electrode tortuosity, we modeled the ion-transport and Li-deposition behaviors in different electrode configurations by using COMSOL software. As exhibited in [Figures 5A](#) and [5B](#), we created simulation cells of 2D channeled electrodes with vertical or horizontal alignments (representing VGA or HGA, respectively) with a current density of 3 mA cm<sup>-2</sup> and features of the electrodes based on experimental samples ([Figure S26](#)). For the vertical electrode, Li ions were transported through the short vertical channels to deposit onto perpendicular walls with a low-tortuosity, direct path ([Figure 5A](#)). As such, the Li-ion concentration dropped by only 2.7% across the electrolyte in the vertical electrode ([Figure 5C](#)). However, in the horizontal electrode, Li ions needed to travel through the limited pores in each horizontal layer to reach the bottom; this highly tortuous path, highlighted by the arrows, extends the length of the ion-transport path and effectively decreases the diffusion limited current density ([Figure 5B](#)). Therefore, a large concentration gradient builds up through the thickness of the horizontal electrode such that the local Li-ion concentration in the electrolyte at the bottom part of the

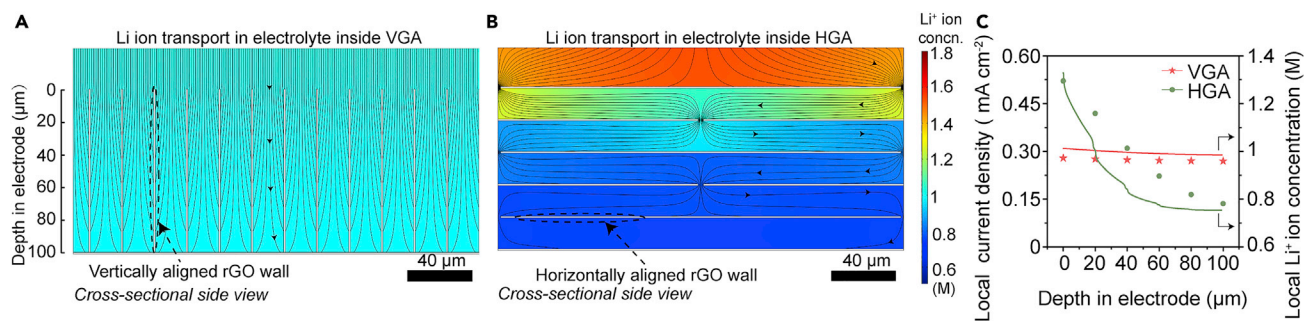


**Figure 5. Simulation Results**

(A and B) Simulation of Li-concentration distribution in (A) low-tortuosity VGA and (B) high-tortuosity HGA electrode configurations. The hole size (averaged  $11\text{ }\mu\text{m}^2$  in size,  $3.3\text{ }\mu\text{m}$  in length) and area ratio (1.32% in area) in rGO layers in HGA were measured from the top-view SEM images of HGA by ImageJ software (Figure S5C). The spacing between adjacent rGO layers was set to  $20\text{ }\mu\text{m}$ , which corresponds with previous SEM images in Figure 2. Color in (A) and (B) denotes concentration, lines show ion-flux streamlines (tangent lines to the electrolyte ionic flux vector field), and the white lines represent rGO sheets. Local streamline number density does not correspond to the ionic current density; it is merely a guide to the eye for visualizing directional ion flux.

(C) Simulated distributions of Li deposition and stripping current density (stars) and concentrations (lines) at different depths in the VGA and HGA electrodes. The current density through the entire cell was fixed at  $3\text{ mA cm}^{-2}$ ; the plotted points are the local current density distributed at the electrode interphase at the specified electrode depth.

electrode is only 56.8% of that at the top. As such, the Li ions consumed at the bottom cannot be replenished fast enough to match the deposition rate, further aggravating uneven Li distribution. Importantly, the top part of the vertical electrode exhibited only a 3.6% higher local current density than the bottom part, demonstrating good homogeneity, whereas the top part of the horizontal electrode showed a 283% higher local current density than the bottom part, suggesting an extremely uneven Li-deposition distribution throughout the electrode as a result of the high tortuosity (Figure 5C). These large variations in electrode current densities in different GA configurations demonstrate that high electrode tortuosity leads to uneven Li-deposition distribution, which is consistent with our previous analyses of Li transport and experimental data.

## Conclusion

In summary, we have demonstrated a significant correlation between electrode tortuosity and the structure evolution and electrochemical reversibility of hosted Li-metal anodes during cycling: high electrode tortuosity significantly aggravates the uneven gradient of ion concentration and electrochemical reactions inside the porous electrode, leading to the dendritic Li-overgrowth issue on the top surface of hosted Li-metal anodes, along with blocked ion transportation and deteriorated electrochemical performances. Through controllable alignment of 2D rGO layers in bulk, the tortuosities of GA electrodes can be regulated over a very large range of values without affecting chemical composition or porosity. The low-tortuosity, vertically aligned rGO electrode achieved a high CE of ~99.08% even under high-capacity and high-current-density cycling conditions ( $5\text{ mAh cm}^{-2}$ ,  $5\text{ mA cm}^{-2}$  in ether electrolyte) and dendrite-free, through-electrode uniform structure in carbonate electrolyte, in addition to 400 stable cycles in a Li-LFP full cell. In comparison, the high-tortuosity rGO electrodes exhibited a severe  $80\text{-}\mu\text{m}$ -thick upper overgrowth of dendrites after a single plating step, rapid anodic CE decay from 98.6% to 90% after only 24 cycles, and fast full-cell failure within 200 cycles with gradually increased electrode tortuosity, even though they had the same chemical composition and porosity. Simulation results reveal that the prolonged ion-transport pathways lead to locally enhanced current density on the upper surface, supporting the experimentally observed tortuosity-aggravated, unevenly

distributed Li-deposition structure throughout tortuous electrodes. Therefore, the significant influence of electrode tortuosity on anode reversibility and morphology can be confirmed. We believe that this new insight into this tortuosity-dependent morphology and reversibility evolution provides not only fundamental understanding on homogenizing ion delivery and stabilizing electrodes for Li-metal anodes but also design guidance for multiple electrochemical reaction systems in the future.

## EXPERIMENTAL PROCEDURES

### Preparation of GA Anodes

First, commercially available GO solution (Hangzhou Gaoxi Technology, 6 mg mL<sup>-1</sup>) was filled into 125-μm-thick polyimide O-ring mold and transferred onto a cold plate. Liquid nitrogen was injected into the cold plate below the mold to achieve vertical or horizontal unidirectional freezing of GO solution (Figure S1). For contrast, the GO solution was immersed into liquid nitrogen for non-oriented freezing. The freezed GO-ice solution was dried under vacuum for 24 h to fabricate the GOA, followed by 600°C annealing in Ar atmosphere to get reduced graphene oxide (GA) aerogel such as the VGA electrode.

### Electrochemistry

Battery cycling performance was evaluated by the galvanostatic cycling of coin cells (CR 2032) with GA working electrodes (1 cm<sup>2</sup>, 0.2 mg cm<sup>-2</sup>). Li-metal foils (Hydro-Québec) were used as the counter electrodes. All GA electrodes used for electrochemical tests were prepared as ultrathin electrodes with thickness around 125 μm, which benefit the electrode volume capacity. For CE cycling tests, one layer of Celgard separators (Celgard 2325, 25 μm thick) was used to separate the working electrode (VGA, HGA, RGA, or Cu) and the counter electrode, and 50 μl electrolyte was added. Two types of electrolyte systems were used: (1) carbonate electrolyte of 1 M LiPF<sub>6</sub> in 1:1 (v/v) EC and DEC (BASF) with 1% VC and 10% FEC as additives and (2) ether electrolyte of 1 M LiTFSI in 1:1 (v/v) DOL/DME electrolyte with 1% LiNO<sub>3</sub> as additive. A 125-μm-thick polytetrafluoroethylene (PTFE) O-ring was used to protect the aligned structure of highly porous GA electrode from being damaged. Battery cycling data were collected with a LAND and an Arbin eight-channel battery tester at room temperature. After assembling and rest for 24 h, coin cells were firstly galvanostatically cycled between 0 and 1 V at 20 μA cm<sup>-2</sup> for 20 cycles (Figures S12D and S14E). Battery cycling was then performed by controlling constant areal capacity for Li plating and cutoff potential for Li stripping during each cycle. The CE was defined as the Li-stripping capacity divided by the Li-plating capacity.

For the LFP||Li full cell, either thin pristine Li foils or a Li-infiltrated GA electrode was employed as the anode together with carbonate electrolyte (1 M LiPF<sub>6</sub> in 1:1 [v/v] EC and DEC [BASF] with 1% VC and 10% FEC as additives). The Li@VGA, Li@RGA, and Li@HGA with limited Li amount here were prepared by electrodepositing 10 mAh capacity of Li metal into GA electrode (1 cm<sup>-2</sup>), followed by cell dissembling and anode reuse. The LFP cathode was prepared by mixing LFP powder (MTI) with polyvinylidene fluoride (MTI) and carbon black (TIMCAL) at a weight ratio of 8:1:1 with N-methyl-2-pyrrolidone (NMP) solvent. The cathode slurry was blade-coated on conductive carbon coated aluminum foil (MTI), calendared, and dried in 80°C vacuum oven before use. The areal mass loading of LFP was ~16 mg cm<sup>-2</sup>. During LFP||Li full cell assembling, one layer of Celgard separators (Celgard 2325, 25 μm thick) was used to separate the anode and cathode. All the LFP||Li batteries were tested between 2.5 and 4 V.

For the NMC622||Li full cell, either thin pristine Li foils or Li-infiltrated GA electrode was employed as anode together with carbonate electrolyte (1 M LiPF<sub>6</sub> in 1:1 [v/v] EC and DEC [BASF] with 1% VC and 10% FEC as additives). The Li@VGA, Li@RGA, and Li@HGA with limited Li amount here were prepared by electrodepositing 5 mAh capacity of Li metal into GA electrode (1 cm<sup>-2</sup>), followed by cell dissembling and anode reuse. A NMC622 cathode was purchased from CANRD with areal mass loading of NMC622 at ~25.6 mg cm<sup>-2</sup> (~4.1 mAh cm<sup>-2</sup>). During NMC622||Li full cell assembling, one layer of Celgard separators (Celgard 2325, 25 µm thick) was used to separate the anode and cathode. All NMC622||Li batteries were tested between 3 and 4.2 V by a constant current-constant voltage charge and constant current discharge protocol.

The electrode tortuosity was measured by both ionic resistance mode and polarization-interruption mode. For ionic resistance mode, the electronic-insulated GOA was placed inside the PTFE O-ring on a stainless-steel electrode, and 20 µL of electrolyte was added. Another stainless steel electrode was covered onto several layers of GOA-embedded PTFE O-ring and assembled as cells (Figure S8E).<sup>35</sup> Electrochemical impedance spectroscopy (EIS) measurements were taken near the open circuit voltage of each cell with appropriate frequency ranges and a 10 mV perturbation. The tortuosity was calculated by the slope in Figure 2I. For polarization-interruption mode, the GOA-embedded PTFE O-ring was placed between two Celgard 2325 separator-coated Li metal, soaked by electrolyte, and assembled into cells.<sup>34,36</sup> The assembled cells were tested with a battery tester. A stable SEI on the Li metal was formed by cycling consisting of passing a constant current (0.5 mA cm<sup>-2</sup>) for 10 min, a 3-min rest period, and then passing current in the reverse direction under the same conditions. After the conditioning cycles, a constant current of 2 mA cm<sup>-2</sup> was applied for 2 min to set up a concentration gradient in the cell. Then, the concentration gradient was allowed to relax by interrupting the current until the cell potential approached zero. Then the current direction was reversed for 2 min followed by interruption of the current until cell potential approached zero. The relaxation of the concentration gradient was observed in terms of a cell-potential decay with the time. Both ionic resistance mode and polarization-interruption mode were repeated several times for accuracy. The thickness of the PTFE O-ring was the same as GA electrodes to keep their aligned structure from being damaged.

### Characterization

SEM images were taken with a FEI XL30 Sirion scanning electron microscope at an acceleration voltage of 5 kV. Before SEM studies of electrodes, batteries were disassembled in an argon-filled glovebox and then gently rinsed with DEC to remove residual salt. The Li-metal coating uniformity in Li@VGA electrodes were measured by cross-sectioning with a Ga<sup>+</sup> ion beam and observing with the electron beam on a FEI Helios NanoLab 600i DualBeam FIB/SEM. XRD patterns were recorded on a PANalytical X'Pert instrument. XPS analysis was obtained on a PHI VersaProbe 1 scanning XPS microprobe with an air-free transfer vessel. The binding energies were calibrated with respect to the C<sub>1s</sub> peak at 284.6 eV. The sputtering process helped to remove the characterized surface from the material layer by layer and exhibited the inner layer. The sputtering rate calibrated by SiO<sub>2</sub> was 4 nm min<sup>-1</sup>. TEM characterization was performed at 300 kV with a FEI Titan TEM. Raman spectra was performed under 532 nm laser excitation (Horiba Labram HR Evolution Raman System) at room temperature.

### SUPPLEMENTAL INFORMATION

Supplemental Information can be found online at <https://doi.org/10.1016/j.joule.2020.03.008>.

## ACKNOWLEDGMENTS

Part of this work was performed at the Stanford Nano Shared Facilities and Stanford Nanofabrication Facility, supported by the National Science Foundation under award ECCS-1542152. This work was partially supported by the Assistant Secretary for Energy Efficiency and Renewable Energy, the Office of Vehicle Technologies, the Battery Materials Research program, and the Battery500 Consortium program of the US Department of Energy. A.P. acknowledges support from the Stanford Graduate Fellowship. Y.L. acknowledges the Intelligence Community Fellowship for funding.

## AUTHOR CONTRIBUTIONS

H.C., A.P., D.L., J.X., and Y.C. conceived the idea for the project. H.C. and J.W. fabricated the electrodes. H.C. conducted the SEM and XPS characterizations. A.P. conducted the COMSOL simulation. H.W. conducted the XRD characterizations. H.C. and H.W. conducted the electrochemical measurements. D.M. and H.S. conducted the SAXS characterization. R.V., Y.L., and W.H. conducted TEM characterization. Y.W. conducted the *in situ* optical microscopy characterization. A.Y. conducted the Raman characterization. H.C., A.P., H.W., and Y.C. wrote the manuscript. All authors discussed the results and commented on the manuscript at all stages.

## DECLARATION OF INTERESTS

The authors declare no competing interests.

Received: December 17, 2019

Revised: February 25, 2020

Accepted: March 11, 2020

Published: April 8, 2020

## REFERENCES

- Armand, M., and Tarascon, J.M. (2008). Building better batteries. *Nature* 451, 652–657.
- Chu, S., and Majumdar, A. (2012). Opportunities and challenges for a sustainable energy future. *Nature* 488, 294–303.
- Goriparti, S., Miele, E., De Angelis, F., Di Fabrizio, E., Proietti Zaccaria, R., and Capiglia, C. (2014). Review on recent progress of nanostructured anode materials for Li-ion batteries. *J. Power Sources* 257, 421–443.
- Liu, Y., Zhou, G., Liu, K., and Cui, Y. (2017). Design of complex nanomaterials for energy storage: past success and future opportunity. *Acc. Chem. Res.* 50, 2895–2905.
- Lin, D., Liu, Y., and Cui, Y. (2017). Reviving the Li metal anode for high-energy batteries. *Nat. Nanotechnol.* 12, 194–206.
- Xu, W., Wang, J., Ding, F., Chen, X., Nasibulin, E., Zhang, Y., and Zhang, J.-G. (2014). Li metal anodes for rechargeable batteries. *Energy Environ. Sci.* 7, 513–537.
- Li, Q., Yi, T., Wang, X., Pan, H., Quan, B., Liang, T., Guo, X., Yu, X., Wang, H., Huang, X., et al. (2019). In-situ visualization of Li plating in all-solid-state Li-metal battery. *Nano Energy* 63, 103895.
- Aurbach, D., Zinigrad, E., Cohen, Y., and Teller, H. (2002). A short review of failure mechanisms of Li metal and lithiated graphite anodes in liquid electrolyte solutions. *Solid State Ionics* 148, 405–416.
- Li, Z., Huang, J., Yann Liaw, B., Metzler, V., and Zhang, J. (2014). A review of Li deposition in Li-ion and Li metal secondary batteries. *J. Power Sources* 254, 168–182.
- Zheng, G., Lee, S.W., Liang, Z., Lee, H.W., Yan, K., Yao, H., Wang, H., Li, W., Chu, S., and Cui, Y. (2014). Interconnected hollow carbon nanospheres for stable Li metal anodes. *Nat. Nanotechnol.* 9, 618–623.
- Lu, Y., Tu, Z., and Archer, L.A. (2014). Stable Li electrodeposition in liquid and nanoporous solid electrolytes. *Nat. Mater.* 13, 961–969.
- Liu, Y., Tzeng, Y.-K., Lin, D., Pei, A., Lu, H., Melosh, N.A., Shen, Z.-X., Chu, S., and Cui, Y. (2018). An ultrastrong double-layer nanodiamond interface for stable Li metal anodes. *Joule* 2, 1595–1609.
- Wang, X., Zhuang, J., Liu, M., Wang, C., Zhong, Y., Wang, H., Cheng, X., Liu, S., Cao, G., and Li, W. (2019). Facile and scalable engineering of a heterogeneous microstructure for uniform, stable and fast Li plating/stripping. *J. Mater. Chem. A* 7, 19104–19111.
- Xia, S., Lopez, J., Liang, C., Zhang, Z., Bao, Z., Cui, Y., and Liu, W. (2019). High-rate and large-capacity Li metal anode enabled by volume conformal and self-healable composite polymer electrolyte. *Adv. Sci.* 6, 1802353.
- Stone, G.M., Mullin, S.A., Teran, A.A., Hallinan, D.T., Minor, A.M., Hexemer, A., and Balsara, N.P. (2012). Resolution of the modulus versus adhesion dilemma in solid polymer electrolytes for rechargeable Li metal batteries. *J. Electrochem. Soc.* 159, A222–A227.
- Fan, X., Chen, L., Borodin, O., Ji, X., Chen, J., Hou, S., Deng, T., Zheng, J., Yang, C., Liou, S.C., et al. (2018). Non-flammable electrolyte enables Li-metal batteries with aggressive cathode chemistries. *Nat. Nanotechnol.* 13, 715–722.
- Zheng, J., Engelhard, M.H., Mei, D., Jiao, S., Polzin, B.J., Zhang, J.-G., and Xu, W. (2017). Electrolyte additive enabled fast charging and stable cycling Li metal batteries. *Nat. Energy* 2, 17012.
- Mauger, A., Julien, C.M., Paoletta, A., Armand, M., and Zaghib, K. (2018). A comprehensive review of Li salts and beyond for rechargeable batteries: progress and perspectives. *Mater. Sci. Eng. R Rep.* 134, 1–21.
- Yan, K., Lee, H.W., Gao, T., Zheng, G., Yao, H., Wang, H., Lu, Z., Zhou, Y., Liang, Z., Liu, Z., et al. (2014). Ultrathin two-dimensional atomic crystals as stable interfacial layer for improvement of Li metal anode. *Nano Lett.* 14, 6016–6022.
- Li, Y., Li, Y., Pei, A., Yan, K., Sun, Y., Wu, C.L., Joubert, L.M., Chin, R., Koh, A.L., Yu, Y., et al. (2017). Atomic structure of sensitive battery

- materials and interfaces revealed by cryo-electron microscopy. *Science* 358, 506–510.
- 21. Yan, K., Lu, Z., Lee, H.-W., Xiong, F., Hsu, P.-C., Li, Y., Zhao, J., Chu, S., and Cui, Y. (2016). Selective deposition and stable encapsulation of Li through heterogeneous seeded growth. *Nat. Energy* 1, 16010.
  - 22. Lin, D., Liu, Y., Liang, Z., Lee, H.W., Sun, J., Wang, H., Yan, K., Xie, J., and Cui, Y. (2016). Layered reduced graphene oxide with nanoscale interlayer gaps as a stable host for Li metal anodes. *Nat. Nanotechnol.* 11, 626–632.
  - 23. Xu, Y., Li, T., Wang, L., and Kang, Y. (2019). Interlayered dendrite-free Li plating for high-performance Li-metal batteries. *Adv. Mater.* 31, e1901662.
  - 24. Liang, Z., Lin, D., Zhao, J., Lu, Z., Liu, Y., Liu, C., Lu, Y., Wang, H., Yan, K., Tao, X., and Cui, Y. (2016). Composite Li metal anode by melt infusion of Li into a 3D conducting scaffold with lithophilic coating. *Proc. Natl. Acad. Sci. USA* 113, 2862–2867.
  - 25. Yang, C.P., Yin, Y.X., Zhang, S.F., Li, N.W., and Guo, Y.G. (2015). Accommodating Li into 3D current collectors with a submicron skeleton towards long-life Li metal anodes. *Nat. Commun.* 6, 8058.
  - 26. Li, Q., Zhu, S., and Lu, Y. (2017). 3D porous Cu current collector/Li-metal composite anode for stable Li-metal batteries. *Adv. Funct. Mater.* 27, 1606422.
  - 27. Paolella, A., Demers, H., Chevallier, P., Gagnon, C., Girard, G., Delaporte, N., Zhu, W., Vijh, A., Guerfi, A., and Zaghib, K. (2019). A platinum nanolayer on Li metal as an interfacial barrier to shuttle effect in Li-S batteries. *J. Power Sources* 427, 201–206.
  - 28. Lin, D., Zhao, J., Sun, J., Yao, H., Liu, Y., Yan, K., and Cui, Y. (2017). Three-dimensional stable Li metal anode with nanoscale Li islands embedded in ionically conductive solid matrix. *Proc. Natl. Acad. Sci. USA* 114, 4613–4618.
  - 29. Wang, H., Lin, D., Liu, Y., Li, Y., and Cui, Y. (2017). Ultrahigh-current density anodes with interconnected Li metal reservoir through overlithiation of mesoporous AlF<sub>3</sub> framework. *Sci. Adv.* 3, e1701301.
  - 30. Ji, X., Liu, D.-Y., Prendiville, D.G., Zhang, Y., Liu, X., and Stucky, G.D. (2012). Spatially heterogeneous carbon-fiber papers as surface dendrite-free current collectors for Li deposition. *Nano Today* 7, 10–20.
  - 31. Liu, Y., Lin, D., Liang, Z., Zhao, J., Yan, K., and Cui, Y. (2016). Li-coated polymeric matrix as a minimum volume-change and dendrite-free Li metal anode. *Nat. Commun.* 7, 10992.
  - 32. Von Lüders, C., Keil, J., Webersberger, M., and Jossen, A. (2019). Modeling of Li plating and Li stripping in Li-ion batteries. *J. Power Sources* 414, 41–47.
  - 33. Harris, S.J., Timmons, A., Baker, D.R., and Monroe, C. (2010). Direct *in situ* measurements of Li transport in Li-ion battery negative electrodes. *Chem. Phys. Lett.* 485, 265–274.
  - 34. Thorat, I.V., Stephenson, D.E., Zacharias, N.A., Zaghib, K., Harb, J.N., and Wheeler, D.R. (2009). Quantifying tortuosity in porous Li-ion battery materials. *J. Power Sources* 188, 592–600.
  - 35. Landesfeind, J., Hattendorff, J., Ehrl, A., Wall, W.A., and Gasteiger, H.A. (2016). Tortuosity determination of battery electrodes and separators by impedance spectroscopy. *J. Electrochem. Soc.* 163, A1373–A1387.
  - 36. Pouraghajian, F., Knight, H., Wray, M., Mazzeo, B., Subbaraman, R., Christensen, J., and Wheeler, D. (2018). Quantifying tortuosity of porous Li-Ion battery electrodes: comparing polarization-interrupt and blocking-electrolyte methods. *J. Electrochem. Soc.* 165, A2644–A2653.
  - 37. Yao, K.P.C., Okasinski, J.S., Kalaga, K., Shkrob, I.A., and Abraham, D.P. (2019). Quantifying Li concentration gradients in the graphite electrode of Li-ion cells using *operando* energy dispersive X-ray diffraction. *Energy Environ. Sci.* 12, 656–665.
  - 38. Ebner, M., Chung, D.-W., García, R.E., and Wood, V. (2014). Tortuosity anisotropy in Li-ion battery electrodes. *Adv. Energy Mater.* 4, 1301278.
  - 39. Billaud, J., Bouville, F., Magrini, T., Villevieille, C., and Studart, A.R. (2016). Magnetically aligned graphite electrodes for high-rate performance Li-ion batteries. *Nat. Energy* 1, 16097.
  - 40. Zhang, H., Hussain, I., Brust, M., Butler, M.F., Rannard, S.P., and Cooper, A.I. (2005). Aligned two- and three-dimensional structures by directional freezing of polymers and nanoparticles. *Nat. Mater.* 4, 787–793.
  - 41. Gutiérrez, M.C., Ferrer, M.L., and del Monte, F. (2008). Ice-templated materials: sophisticated structures exhibiting enhanced functionalities obtained after unidirectional freezing and ice-segregation-induced self-assembly. *J. Chem. Mater.* 20, 634–648.
  - 42. Mahler, W., and Bechtold, M.F. (1980). Freeze-formed silica fibres. *Nature* 285, 27–28.
  - 43. Sun, H., Xu, Z., and Gao, C. (2013). Multifunctional, ultra-flyweight, synergistically assembled carbon aerogels. *Adv. Mater.* 25, 2554–2560.
  - 44. Chen, H., Guo, F., Liu, Y., Huang, T., Zheng, B., Ananth, N., Xu, Z., Gao, W., and Gao, C. (2017). A defect-free principle for advanced graphene cathode of aluminum-ion battery. *Adv. Mater.* 29, 28112843.
  - 45. Wu, L., Ohtani, M., Takata, M., Saeki, A., Seki, S., Ishida, Y., and Aida, T. (2014). Magnetically induced anisotropic orientation of graphene oxide locked by *in situ* hydrogelation. *ACS Nano* 8, 4640–4649.
  - 46. Xia, Y., Mathis, T.S., Zhao, M.Q., Anasori, B., Dang, A., Zhou, Z., Cho, H., Gogotsi, Y., and Yang, S. (2018). Thickness-independent capacitance of vertically aligned liquid-crystalline MXenes. *Nature* 557, 409–412.
  - 47. Zhang, W.-J. (2011). Structure and performance of LiFePO<sub>4</sub> cathode materials: a review. *J. Power Sources* 196, 2962–2970.
  - 48. Shi, F., Pei, A., Vailionis, A., Xie, J., Liu, B., Zhao, J., Gong, Y., and Cui, Y. (2017). Strong texturing of Li metal in batteries. *Proc. Natl. Acad. Sci. USA* 114, 12138–12143.